Journal of Hazardous Materials 180 (2010) 566–576

Contents lists available at ScienceDirect

Journal of Hazardous Materials

journal homepage: www.elsevier.com/locate/jhazmat

Adsorption of diethylchlorophosphate on metal oxide nanoparticles under static conditions

Amit Saxena [a], Harsha Mangal [a], P.K. Rai [a,*], A.S. Rawat [a], Vivek Kumar [a], Monika Datta [b]

[a] Centre for Fire, Explosive and Environment Safety, Timarpur, Delhi 110054, India
[b] Department of Chemistry, University of Delhi, Delhi 110006, India

ARTICLE INFO

Article history:
Received 25 January 2010
Received in revised form 14 April 2010
Accepted 15 April 2010
Available online 22 April 2010

Keywords:
Metal oxide nanoparticles
Diethylchlorophosphate
Adsorption kinetics
Degradation

ABSTRACT

Nanoparticles of MgO, Al_2O_3, CaO and SiO_2 were synthesized using aerogel route, and characterized by N_2-BET, SEM, TEM, XRD, TGA and FT-IR techniques. Characterization indicated 2–75 nm diameter nanoparticles with 135–887 m^2/g surface area and microporous–mesoporous characteristics. Prepared nanoparticles were tested for their adsorptive potential by conducting studies on kinetics of adsorption of diethylchlorophosphate under static conditions. The kinetic parameters such as equilibration constant, equilibration capacity, diffusional exponent and adsorbate–adsorbent interaction constant have been determined using linear driving force model and Fickian diffusion model. AP-MgO and AP-CaO showed the maximum (1011 mg/g) and minimum (690 mg/g) uptake of DEClP, respectively. All nanoparticles showed the values of diffusional exponent to be >0.5, indicating the diffusion mechanism to be anomalous. Hydrolysis reaction (identified using GC/MS technique) was found to be the route of degradation of DEClP.

1. Introduction

Diethylchlorophosphate (DEClP), a toxic air pollutant [1] has widely been used for the synthesis of insecticides and as simulant of highly toxic nerve agents [2]. In order to detoxify such toxicants without endangering the human life or the environment, the important way is to utilize suitable material, which can perform the function of both physisorption followed by chemisorption, i.e., initially the adsorbate molecules are physically adsorbed then they follow dissociative chemisorption to such an extent that the chemical integrity of the adsorbate molecule is completely destroyed [1–7].

Nanoparticles of metal oxides have received enormous interest in recent years because of their unique physical and chemical properties [8]. These high surface area materials have been synthesized via soft chemistry by sol–gel process [8], which is the most common and widely used "bottom-up" wet chemical method. First, Utamapanya et al. [9] in 1991 described the modified hypercritical drying process for the preparation of inorganic metal oxide nanoparticles by sol–gel process utilizing aerogel route. Fig. 1 provides a schematic detail of the synthetic procedure in general. Remarkable contributions have been made by Klabunde [3,4,8,9] for the preparation, characterization and application of nanosize metal oxide particles alone and in association with other oxides. These metal oxide nanoparticles have shown promising results for the degradation of toxic chemicals [3–8]. Adsorption and destruction of chlorinated hydrocarbons on metal oxide nanoparticles have been studied [3,4]. Klabunde co-workers [5] have discussed the most appropriate solid sorbents based matrix for the removal of toxicants. Kinetics of adsorptive removal of DEClP and sarin on impregnated Al_2O_3 nanoparticles have also been discussed by Saxena et al. [6]. In order to find out reaction products these either have to be investigated directly using MAS-NMR technique [7] or by extracting them in organic solvent and analyzing through GC–MS [6,10–12]. Literature indicates that nano-crystals of metal oxides can degrade DEClP via hydrolysis to diethylphosphate and tetraethylpyrophosphate [6].

Air contaminated with toxicants can be made breathable by allowing it to come in contact with nanoparticles based systems under dynamic (flow of gas) or static (no flow of gas) conditions. Under static conditions kinetics of adsorption and diffusion of adsorbate over adsorbent have widely been investigated [10–14]. Several researchers have used various models, such as Fickian [15], linear driving force (LDF) [16], a combined barrier resistance/Fickian diffusion and Langmuir type second order kinetics [17] to describe the adsorption kinetics in porous materials and carbon molecular sieves [18]. Saxena et al. [10–12] have also studied the kinetics of adsorption of toxicants in gas phase on carbons and nanoparticles under static conditions and determined various

* Corresponding author. Tel.: +91 011 23907126; fax: +91 011 23819547.
E-mail addresses: amsa888@rediffmail.com (A. Saxena), pramrai@rediffmail.com (P.K. Rai).

0304-3894/$ – see front matter © 2010 Elsevier B.V. All rights reserved.
doi:10.1016/j.jhazmat.2010.04.071

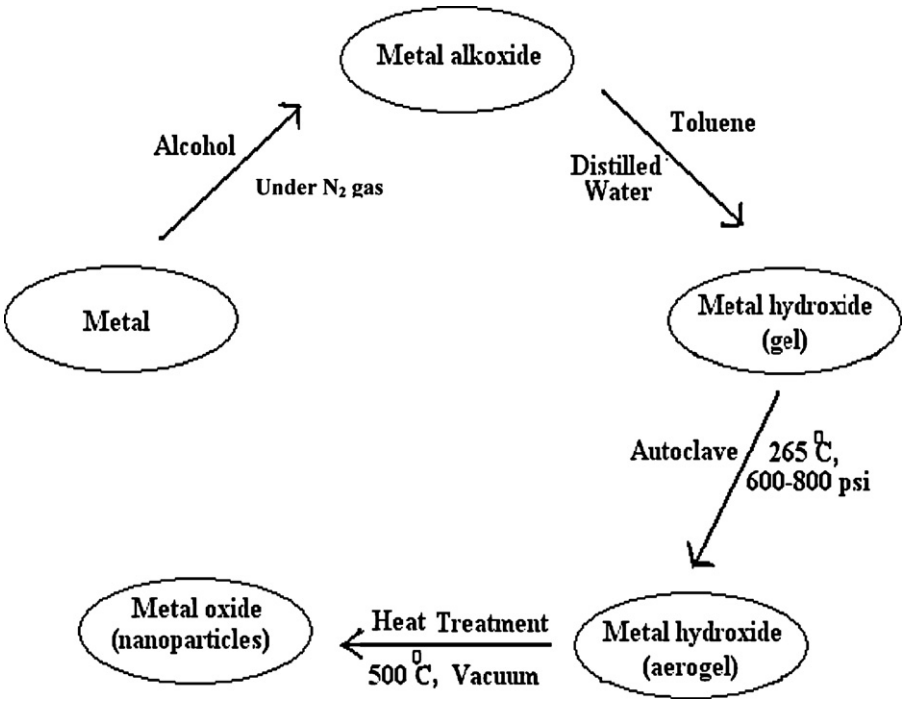

Fig. 1. General schematic for the synthesis of metal oxide nanoparticles.

kinetics parameters such as equilibration time (t), equilibration capacity (M_t), rate constant (k), diffusional exponent (n) and constant (K).

It is always recommended to study with simulant of toxic agents, as simulants are less toxic and their use involves low risk than actual agents. Therefore, in the present study nanoparticles have been synthesized and explored to study the adsorption kinetics of DEClP (a less toxic simulant [2] of toxic organophosphorus compounds, e.g., pesticides and nerve agents). The objective of the present study was to identify the best nanoparticles to remove DEClP and to understand mass transfer phenomena, mode of diffusion and adsorption characteristics on prepared nanoparticles. Suitable nanoparticles can be used in handy decontamination devices to remove toxicants such as pesticldes and nerve agents.

2. Experimental

2.1. Synthesis of nanoparticles

In order to synthesize AP-MgO (AP-Aerogel Process, first introduced by Prof. Kenneth J. Klabunde) nanoparticles 10.0 g of magnesium turnings cleaned with acetone immediately before the reaction was taken with 540 mL of methanol in 1000-mL round-bottom flask and connected to water condenser. One crystal of iodine was also added to catalyze the reaction [19]. The reactants were stirred at room temperature for 24 h under inert atmosphere of nitrogen gas. To this 500 mL of toluene was added and the solution was stirred for 30 min. A solution of stoichiometric amount, i.e., 15 mL (0.8 M) of triple distilled and deionized water in 265 mL of methanol and 775 mL of toluene was prepared. This solution was slowly added to the solution made in earlier with vigorous stirring in a 3.0 l round-bottom flask. The solution was covered with aluminum foil and stirred for 24 h. This resulted in to slightly milky liquid like-gel (Fig. 2a).

600 mL of thus produced magnesium hydroxide gel was transferred to 1000 mL capacity parr autoclave. The gel was first flushed with nitrogen, and the reaction was carried out under nitrogen, with an initial pressure of 100 psi. The reactor was slowly heated from room temperature to 265 °C at the rate of 1 °C/min. The reactor was maintained at 265 °C for 10 min and the system was quickly vented to the atmosphere for over a 1 min period, the furnace taken off and the magnesium hydroxide flushed with nitrogen for 15 min to remove the remaining solvent vapors. This produced fluffy white powder of AP-$Mg(OH)_2$ (Fig. 2b).

20 g of thus produced nano-magnesium hydroxide powder was placed in 500 mL capacity thermal reactor. This was evacuated for 30 min at room temperature. Later, it was slowly heated for 6 h from room temperature to 500 °C under dynamic vacuum of 10^{-2} Torr and kept under this condition for 10 h. This resulted in to the fine white powdery AP-MgO. Finally, the material was cooled to room temperature under vacuum, flushed with nitrogen and stored in air tight bottles till further use. Similar procedure was adopted for the synthesis of CaO [8,20], MgO [21], SiO_2 [11] and Al_2O_3 [12] nanoparticles.

2.2. Characterization of prepared nanoparticles

2.2.1. Surface area and porosity

Surface area and pore size distribution of AP (aerogel produced nanoparticles) hydroxides/oxides and CM (commercially available metal oxide particles) were determined using Autosorb-1-C from Quantachrome, USA. The samples were first outgassed under dynamic vacuum (10^{-2} Torr) for 8 h at 200 °C and then allowed to cool to room temperature. After that, the N_2 adsorption–desorption isotherms were obtained at liquid nitrogen temperature, i.e., 77 K. Surface area and micropore volume were determined using Brunauer–Emmet–Teller (BET) and Dubinin Radushkevich (DR) methods, respectively. Cumulative desorption pore volume was determined using Barrett–Joyner–Halenda (BJH) method. Pore maxima for micro- (<2 nm) and meso- (2–50 nm) pores were determined considering BJH and DFT (density functional theory) methods. The surface area, micropore volume, cumulative desorption pore volume and pore maxima for micropores and mesopores for all prepared nanoparticles and commercial particles have been given in Table 1. Figs. 3 and 4 describe the nitrogen adsorption

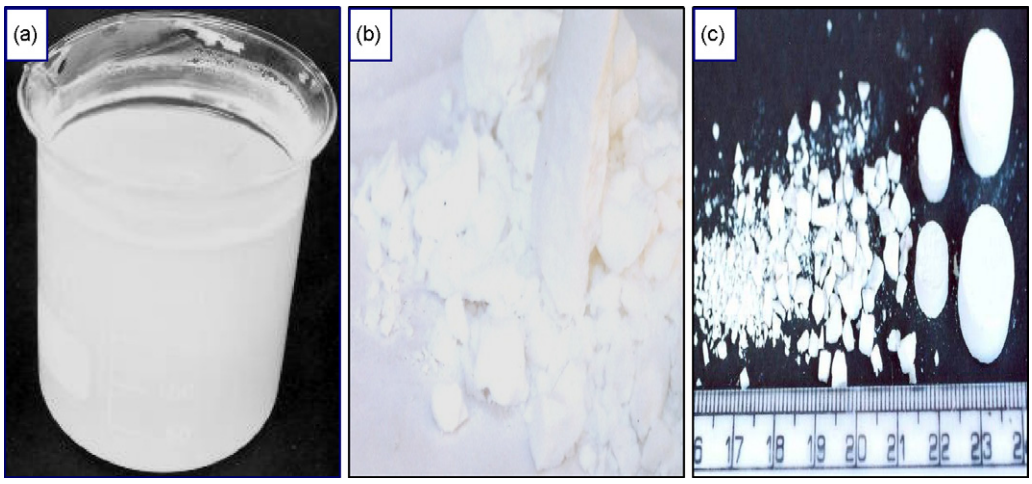

Fig. 2. (a) AP-$Mg(OH)_2$ gel, (b) fluffy AP-$Mg(OH)_2$ after supercritical drying and (c) powder, granules and pellets of prepared AP-MgO nanoparticles.

Table 1
Surface area and pore size distribution of AP-metal hydroxides and oxides and CM metal oxides.

Metal hydroxide/oxide	Surface area (N_2-BET) (m^2/g)	Micropore volume (N_2 DR) (cm^3/g)	Cumulative desorption pore volume (N_2 BJH) (cm^3/g)	Pore maxima for micro- and mesopores (Å)	
				Micro	Meso
AP-$Mg(OH)_2$	904.8	0.289	1.795	18.3	43.8
AP-MgO	407.8	0.117	0.702	17.4	31.4
CM-MgO	45.5	0.019	0.081	11.6	46.2
AP-$Al(OH)_3$	563.2	0.207	1.118	8.2	34.5
AP-Al_2O_3	375.7	0.161	0.571	15.3	27.5
CM-Al_2O_3	105.8	0.043	0.161	13.9	31.5
AP-$Ca(OH)_2$	148.9	0.035	0.223	17.4	30.4
AP-CaO	134.8	0.035	0.186	18.3	32.4
CM-CaO	42.1	0.013	0.061	17.2	30.8
AP-SiO_2	887.3	0.386	1.451	14.6	27.5
CM-SiO_2	389.2	0.178	0.696	11.6	41.7

isotherms and pore size distributions of AP-$Mg(OH)_2$, AP-MgO and CM-MgO.

2.2.2. Scanning electron microscopy/transmission electron microscopy and X-ray diffraction

For SEM characterization, the powder samples were first mounted on brass stubs using double sided adhesive tape and then gold coated for 8 min using ion sputter JEOL, JFC 1100 coating unit. The surface texture of metal oxide nanoparticles was observed using FEI ESEM Quanta 400. Figs. 5 and 6 represent the SEM images of AP-$Mg(OH)_2$ and AP-MgO, respectively.

TEM studies were performed to find out the particle size of the synthesized magnesium hydroxide and oxide nanoparticles. For that 10 mg of AP-$Mg(OH)_2$ powder sample was mixed in 10 mL of pentane and sonicated for 2 h to achieve a better separation of the particles. A drop of supernatant of the solution was placed on the copper grid of 200 mesh size followed by carbon coating. TEM images were recorded using JEOL, JEM-1200 Ex. Figs. 7 and 8

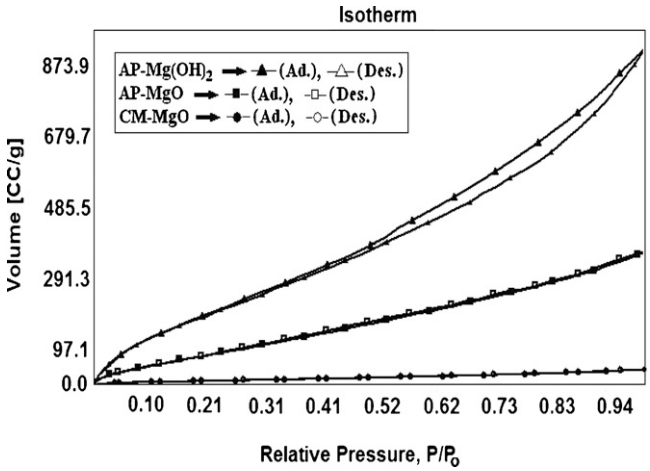

Fig. 3. Adsorption isotherms of AP-$Mg(OH)_2$, AP-MgO and CM-MgO.

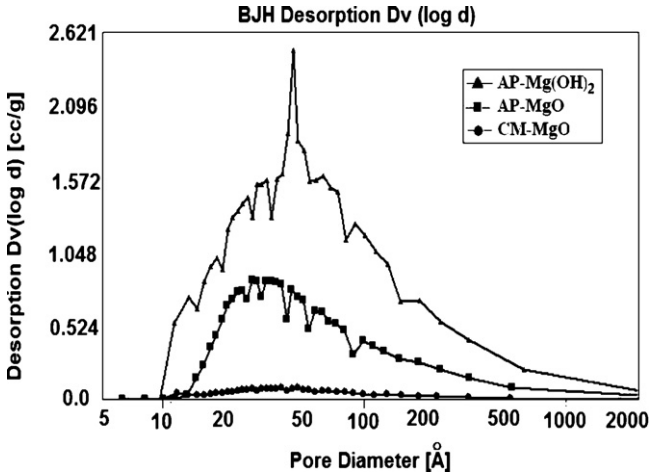

Fig. 4. BJH pore size distributions of AP-$Mg(OH)_2$, AP-MgO and CM-MgO.

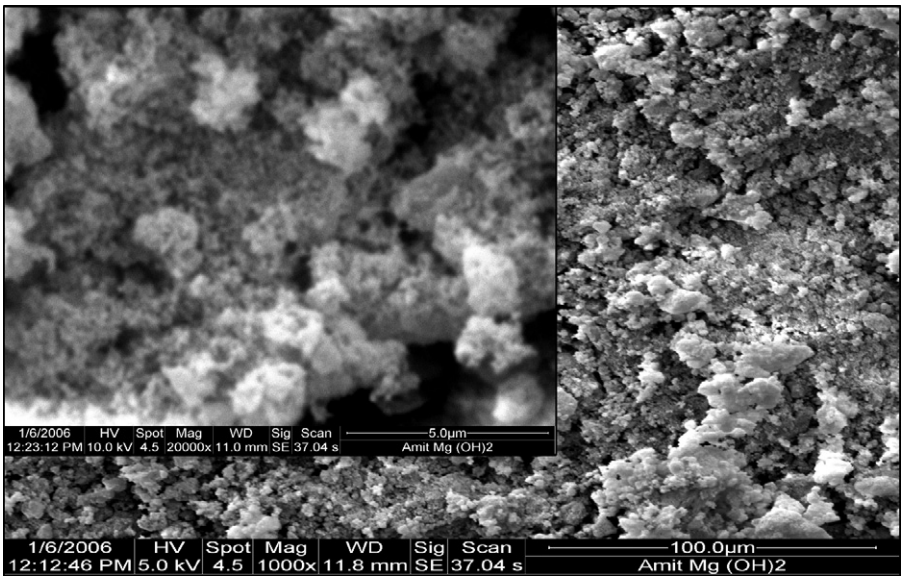

Fig. 5. SEM of AP-$Mg(OH)_2$.

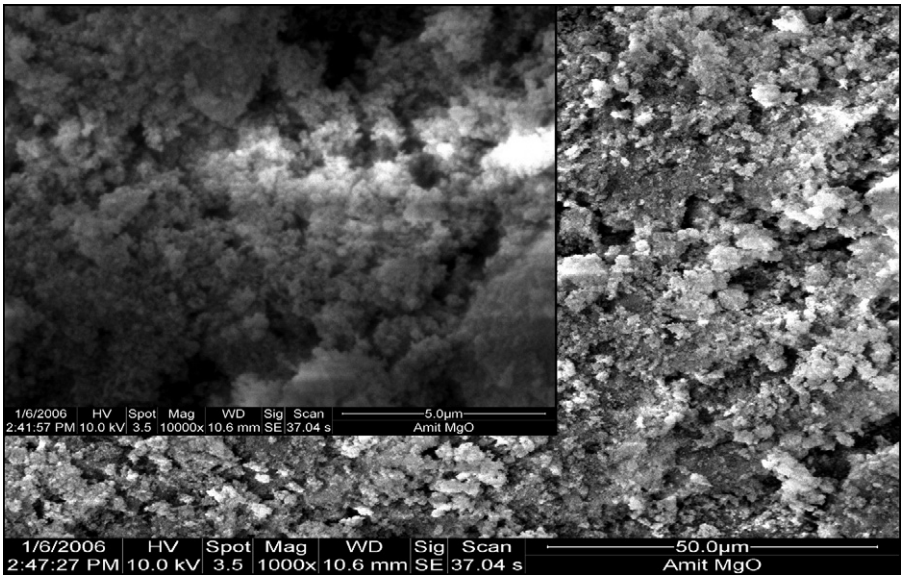

Fig. 6. SEM of AP-MgO.

represent the images of AP-$Mg(OH)_2$ and AP-MgO, respectively. Figs. 9–11 represent the TEM images of AP-Al_2O_3, AP-SiO_2 and AP-CaO, respectively. Imaging at different scales was performed to estimate correctly the proportion of small particles (10–60 nm) embedded in agglomerates (30–200 nm) and the proportion of large particles (120–200 nm). Further more, the particles overlapping in agglomerates lead to quite noisy images making the determination of proportion and size of the smallest particle population a very difficult task.

For XRD studies the powder samples were heat treated under vacuum before placing onto the sample holder. The instrument used was Philips XRD PW 3020. Cu Kα radiation ($\lambda = 0.154$ nm) was the light source used with applied voltage of 40 kV and current of 40 mA. The 2θ angles ranged from 20° to 80° with a speed of 0.05°/s. The crystallite size was then calculated from the XRD spectra using Scherrer equation. Fig. 12 shows the XRD pattern of AP-$Mg(OH)_2$ and AP-MgO. Table 2 describes the particle diameter on the basis of TEM and XRD.

2.2.3. Fourier transform infra-red spectroscopy and thermogravimetric analysis

Fourier transform infra-red study of nanoparticles was performed to find out the complete solvent removal after heat treatment. For that a few of the particles of powder nanosize $Mg(OH)_2$ was mixed with 200 mg of potassium bromide, ground to make pellets, dried and finally recorded the IR spectra (Fig. 13).

Table 2
Nanoparticle diameter based on XRD and TEM.

Metal hydroxide/oxide	D_{TEM} (nm)	D_{XRD} (nm)
AP-$Mg(OH)_2$	4–20 (10)	6–17 (17)
AP-MgO	6–35 (25)	6–13 (7)
AP-$Al(OH)_3$	4–30 (20)	2–15 (3)
AP-Al_2O_3	3–14 (10)	2–17 (4)
AP-$Ca(OH)_2$	18–50 (30)	8–17 (17)
AP-CaO	8–40 (26)	12–24 (23)
AP-SiO_2	24–75 (36)	2–27 (2)

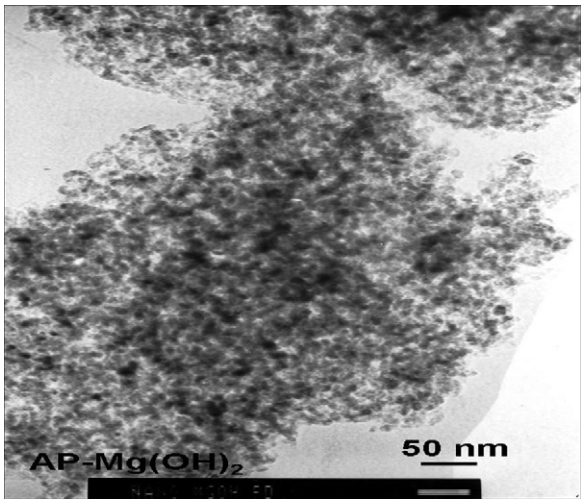

Fig. 7. TEM of AP-$Mg(OH)_2$.

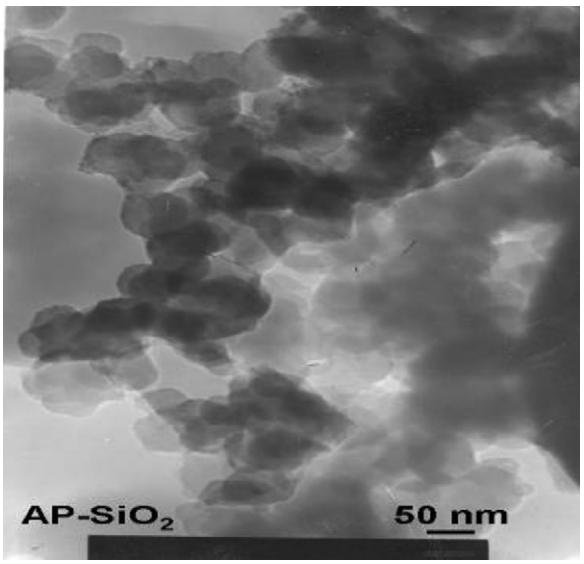

Fig. 10. TEM of AP-SiO_2.

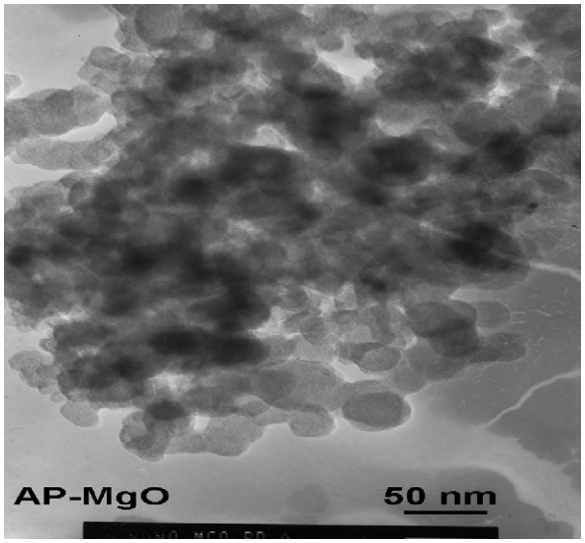

Fig. 8. TEM of AP-MgO.

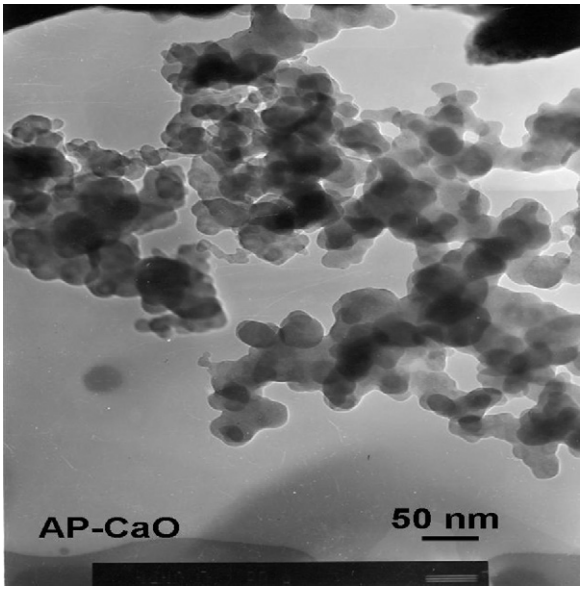

Fig. 11. TEM of AP-CaO.

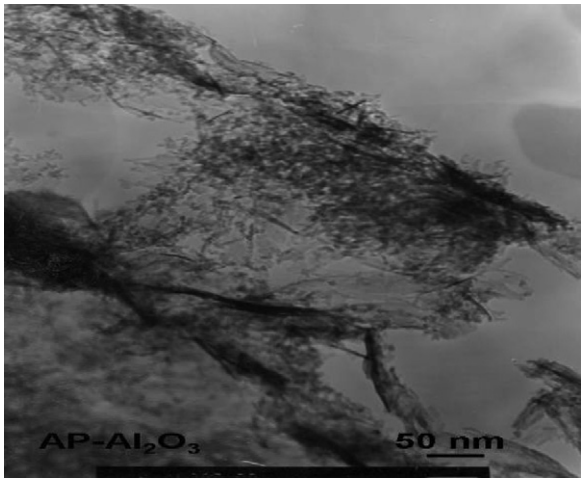

Fig. 9. TEM of AP-Al_2O_3.

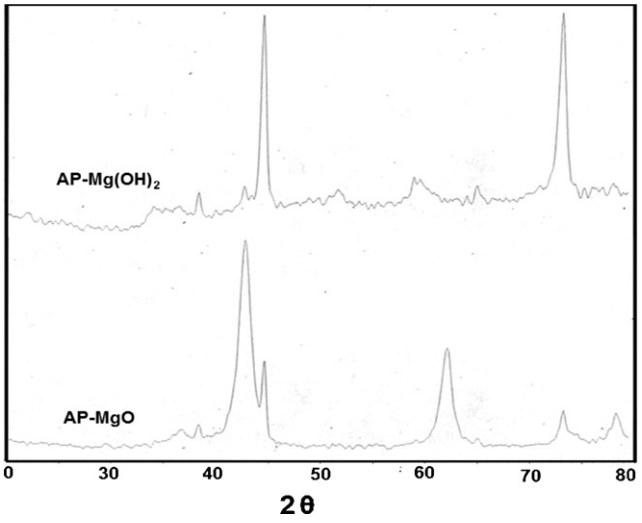

Fig. 12. XRD pattern of AP-$Mg(OH)_2$ and AP-MgO.

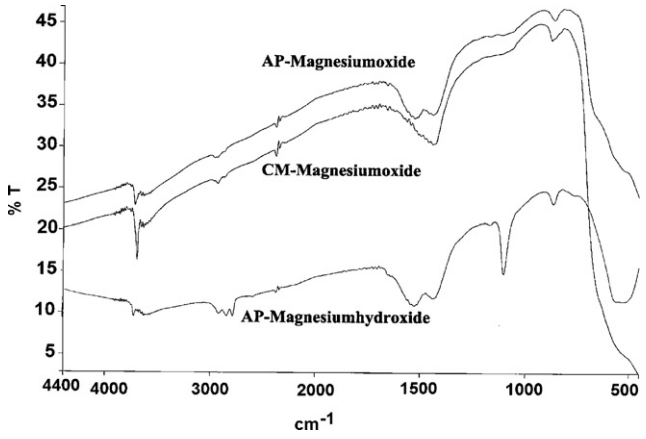

Fig. 13. FT-IR of AP-$Mg(OH)_2$, AP-MgO and CM-MgO.

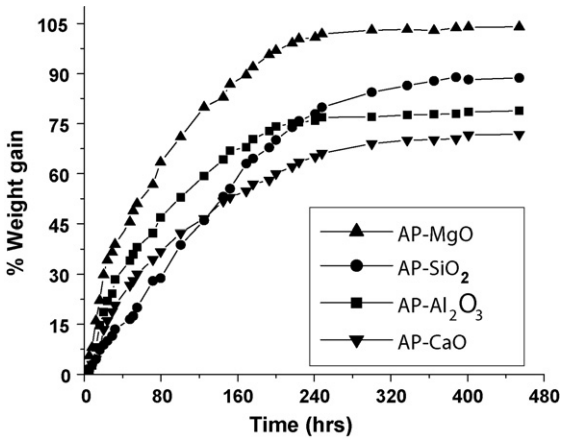

Fig. 15. Kinetics of uptake of DEClP on prepared nanoparticles.

TGA was used to study the conversion of nanoparticles of metal hydroxide to metal oxides and make a comparison with commercial metal oxides. Thermograms for materials were recorded from 30 to 800 °C in air using thermogravimetric analyzer, TGA-2950 from TA Instruments, USA. The initial sample weight was always 10 mg and the heating rate was 20 °C/min. Fig. 14 shows the TGA profile.

2.2.4. Bulk density and moisture content

The bulk density of synthesized and commercial materials were measured by weighing a known volume (20 mL) of material and expressed in g/mL. The moisture content of the material was determined by heating a known amount (1 g) of sample in oven at 120 °C for 6 h, cooling in desiccators for 1 h and finally weighing. The weight loss per 100 g sample was taken as moisture content of the material. The bulk density and moisture content results have been described in Table 3. All above given characterization was also done for AP-Al_2O_3, AP-SiO_2 and AP-CaO nanoparticles.

2.3. Static adsorption studies

In order to carry out the adsorption of DEClP under static conditions, 100 mg each of nanoparticles was taken separately in gooch crucibles and placed on perforated disc in a closed glass chamber in which 5.0 mL of DEClP was placed at the bottom of chamber. To maintain constant temperature, the glass chamber along with weighing balance was housed in an oven kept at 35 ± 1 °C. The kinetics of adsorption of DEClP was studied by monitoring the percentage of weight gain every hour. The possibility of co-adsorption of atmospheric moisture available in the closed chamber cannot be ruled out; however, the co-adsorption of atmospheric moisture will be insignificant and will not affect the adsorption of DEClP due to very little influence of humidity on adsorption of toxicants [22]. In a control experiment when adsorbents were exposed to the ambient air moisture of the chamber to the same period of time, the adsorption was less than 2.5% with all studied systems.

Of the above; the concentration of gas was considered to be constant at atmospheric pressure in the glass chamber. As the adsorption of toxicant by the nanoparticles based adsorbents starts it causes the depletion in vapor phase concentration of toxicant in the glass chamber. The depletion in concentration is compensated by liquid phase toxicant, which was placed at the bottom of the glass chamber. Therefore, the concentration of toxicant vapor in the glass chamber remains constant and it ensures a continuous supply of toxicant to the adsorbent. Figs. 15–17 represent the kinetics of uptake, diffusion and adsorption of DEClP on prepared nanoparticles, respectively. Table 4 represents the kinetics parameters.

2.4. Identification of reaction products

In order to investigate the reaction products 10 mg of DEClP exposed nanoparticles were extracted with 2.0 mL of acetonitrile for 2 h in a well stoppered test tube. The extracts were centrifuged,

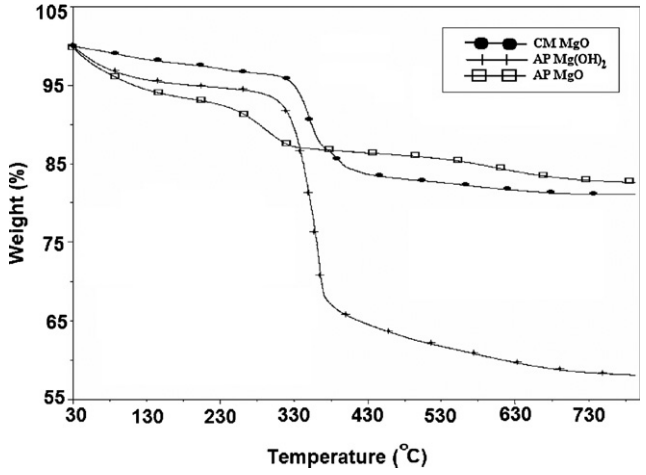

Fig. 14. Thermograms of AP-$Mg(OH)_2$, AP-MgO and CM-MgO.

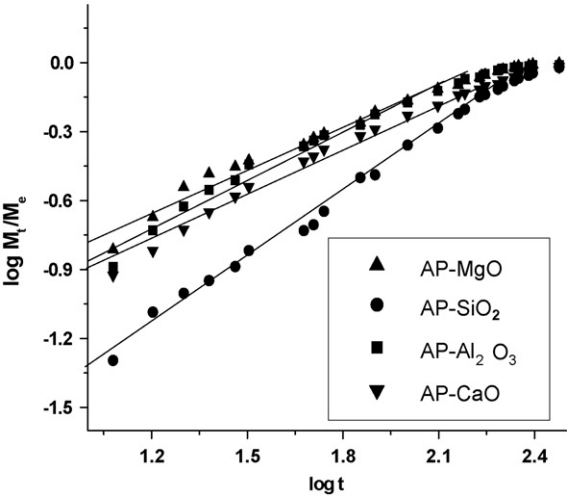

Fig. 16. Kinetics of diffusion of DEClP on prepared nanoparticles.

Table 3
Acid neutralization capacity, bulk density and moisture content of AP-metal hydroxides and oxides and CM metal oxides.

Metal hydroxide/oxide	pH reached	Acid/base neutralization capacity (mmol/mol of metal oxide)	Bulk density (g/mL)	Moisture content (%)
AP-$Mg(OH)_2$	11.4	1380.4 HCl	0.026	1.6
AP-MgO	11.5	1532.3 HCl	0.054	0.9
CM-MgO	11.2	1591.8 HCl	0.209	4.2
AP-$Al(OH)_3$	5.68	5.6 NaOH	0.046	1.9
AP-Al_2O_3	6.6	2.9 HCl	0.043	0.6
CM-Al_2O_3	7.6	8.85 HCl	0.897	3.4
AP-$Ca(OH)_2$	11.9	1386.5 HCl	0.072	2.1
AP-CaO	11.7	911.6 HCl	0.098	1.2
CM-CaO	12.4	1515.4 HCl	0.525	2.6
AP-SiO_2	5.9	3.3 NaOH	0.035	0.8
CM-SiO_2	6.1	1.5 NaOH	0.573	2.3

Table 4
Kinetics parameters for the adsorption of DEClP on prepared nanoparticles.

Metal oxide	Equilibration time (h)	Equilibration capacity (mg/g)	Diffusional exponent (n)	Constant (K) (h^{-1})	Rate constant (k) (h^{-1}) $\times 10^{-3}$
AP-MgO	246	1011	0.67	0.17	11.5
AP-SiO_2	380	885	0.94	0.05	6.8
AP-Al_2O_3	252	770	0.71	0.14	13.6
AP-CaO	296	690	0.64	0.13	8.0

transferred to another tube and purged with nitrogen gas to concentrate the extracted reaction products and finally subjected to product identification using GC/MS (gas chromatograph coupled with mass spectrometer) instrumental techniques. GC/MS (6890N GC coupled with 5973 inert MS detector) of Agilent Technologies, USA was used for characterization of reaction products. It was equipped with HP-5 MS column of 30 m × 0.25 mm × 0.25 μ dimensions. Temperature programming [50 °C (2 min hold) to 280 °C (10 min hold) @ 10 °C/min] with split injection technique (10:1) was used to perform the study. Injection port and GC/MS interface, MS source and quadrupole analyzer were kept at 280, 230 and 150 °C, respectively. The mass spectra of reaction products were compared with the standard mass spectra (Figs. 18 and 19) from existing libraries (Wiley and NIST) of GC/MS instrument.

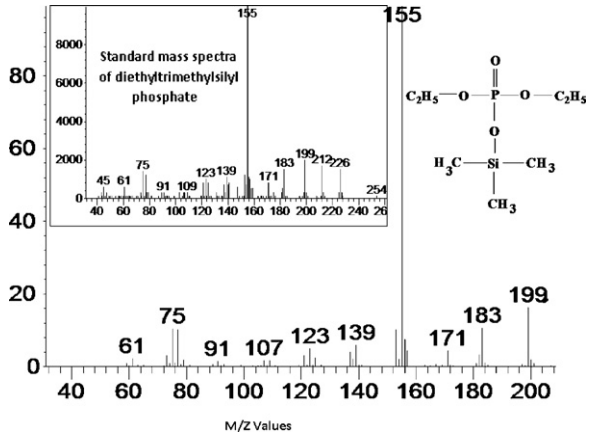

Fig. 18. Comparative mass spectra of product and standard diethyltrimethylsilyl phosphate.

3. Results and discussion

3.1. Characterization of prepared nanoparticles

Nitrogen adsorption–desorption isotherms and BJH pore size distributions of AP-$Mg(OH)_2$, AP-MgO and CM-MgO have been rep-

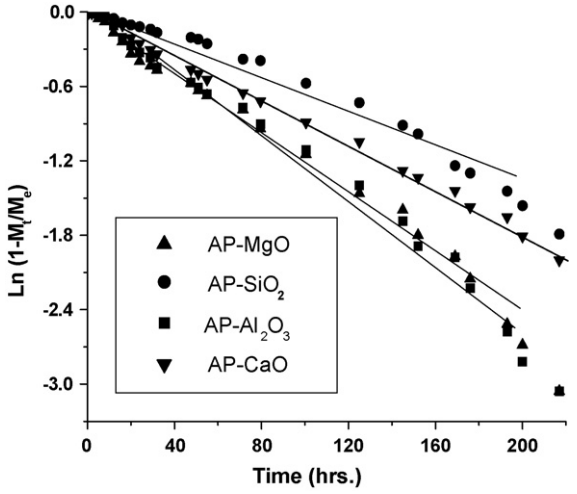

Fig. 17. Kinetics of adsorption of DEClP on prepared nanoparticles.

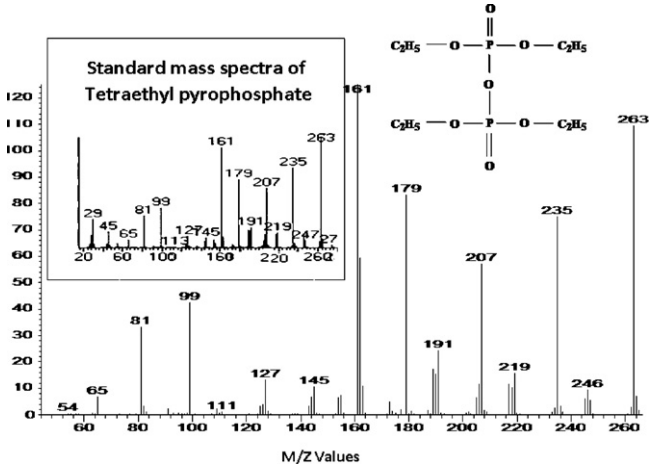

Fig. 19. Comparative mass spectra of product and standard tetraethyl pyrophosphate.

resented in Figs. 3 and 4. AP-$Mg(OH)_2$ showed highest uptake of nitrogen and exhibited broad hysteresis loop, which are characteristic of adsorption possessing a high portion of mesopores, however, such type of broad hysteresis was not observed with AP and CM-MgO. Fig. 4 clearly indicated that AP-$Mg(OH)_2$, AP-MgO and CM-MgO have the similar type of pore size distributions with mesopore maxima at 43.8, 31.4 and 46.2 Å (Table 1), respectively. Apart from mesoporous characteristic AP-$Mg(OH)_2$ and AP-MgO were also found to be having micropores with micropore maxima at 18.3 and 17.4 Å, respectively. The surface area of AP-$Mg(OH)_2$ was found to be 904.8 m^2/g, whereas, Diao et al. [23] have indicated it to be maximum 1011 m^2/g. On heat treatment of AP-$Mg(OH)_2$ to AP-MgO at 500 °C the surface area decreased to 407.8 m^2/g (Utamapanya et al. [9] have indicated it to be 219–522 m^2/g). This decrease was due to the dehydration process, which causes severe sintering and damage to the pore structure [9]. Micropore and cumulative desorption pore volume of AP-MgO were also found to be decreasing to 40% of AP-$Mg(OH)_2$. The decrease is almost similar as that of surface area (45%). The ratio of cumulative desorption pore volume to micropore volume was also found to be similar (~6.0%) for AP-$Mg(OH)_2$ and AP-MgO. Surface area of AP-MgO was found to be nine times of that of the material commercially available (CM-MgO).

On heat treatment of AP-$Al(OH)_3$ to AP-Al_2O_3 the surface area decreased from 563.2 to 375.7 m^2/g. This decrease was found to be lesser than the decrease associated with AP-$Mg(OH)_2$ to AP-MgO. AP-$Al(OH)_3$ has shown 8.2 Å as micropore maxima. AP-$Ca(OH)_2$ and AP-CaO have shown the lowest values of surface area and pore volumes (Table 1) among synthesized nanoparticles. AP-SiO_2 has shown 887.3 m^2/g surface area. CM-SiO_2 has strongly indicated the mesopore maxima to be 41.7 Å; however, AP-SiO_2 has indicated wide pore size distributions in mesoporous range. All synthesized nanoparticles have shown the comparable values for surface area and pore volumes in relation to the reported literature.

Moreover, Figs. 5–11 show the SEM and TEM images of AP-metal hydroxide and oxides. Table 2 indicates the particle diameter (in reference to TEM images) in nm for synthesized nanoparticles. SEM images of AP-$Mg(OH)_2$ (Fig. 5) and AP-MgO (Fig. 6) indicated the material to be having a multitude of thin strands to give fluffy and porous web like structure with wide particle size distributions. TEM images of AP-$Mg(OH)_2$ (Fig. 7) and AP-MgO (Fig. 8) indicated these materials consisting of weblike structure [8,9] with the particle diameter in the range of 4–20 nm (maximum particles of 10 nm diameter) and 6–35 nm (maximum particles of 25 nm diameter), respectively. Imaging at different scales was performed to estimate correctly the proportion of small particles (2–10 nm) and embedded in agglomerates (10–100 nm). Synthesized nanoparticles showed the decrease in particle diameter on conversion from hydroxides to oxides. Smallest particles were of 4 nm diameter, however, three to four crystallites aggregate in to ~10 nm particles, and these particles weakly agglomerate in to a mass with large pores, where the pores are actually the space between the particles (as opposed to holes and channels in the particles themselves). TEM image of AP-SiO_2 (Fig. 10) indicated the particles of 24–75 nm, mostly, however, were observed to be 36 nm in size. Crystallite size of AP-$Ca(OH)_2$ was found to be 18–50 nm [mainly 30 nm (Table 2)], which decreased during conversion of AP-$Ca(OH)_2$ to AP-CaO, yielding 8–40 nm [mainly 26 nm (Table 2 and Fig. 11)] particles. Decrease in crystallite size on metal hydroxide to metal oxide conversion has also been reported by Klabunde [8]. He has also indicated the crystallite aggregate size to ~25 nm. Except AP-MgO nanoparticles all these materials have shown a decrease in particle diameter on conversion from hydroxides to oxides.

The crystallites sizes of the synthesized nanoparticles were also calculated from the line broadening of the peak, using the Scherrer equation; in Table 2. XRD spectra of AP-$Mg(OH)_2$ and AP-MgO indicated an amorphous pattern due to peak broadening with the particle diameter in the range of 6–17 nm (Fig. 12). A rough estimation of AP-$Mg(OH)_2$ peak broadening at 59 (2θ) indicated the particle diameter to be 6.3 nm, and as per highest reflex at 44 and 73 (2θ) it was found to be 17 and 13 nm, respectively (Table 2 and Fig. 12). However, literature [4,9] suggests the particle diameter to be 2.1–8.8 nm. Crystallite size of AP-MgO was found to be 6–13 nm [mainly 7 nm for reflex at $2\theta = 42$]. XRD spectrum of AP-MgO was also found to be similar to that of reported by Utamapanya et al. [9]. Distorted peaks at 2θ values near to 37° and 59° indicate the presence of amorphous $Mg(OH)_2$. In addition to this a small decaying peak at 2θ value near to 33° indicates the presence of $Mg(OH)(OCH_3)$ suggesting that the hydrolysis is only completed partially even when a stoichiometric amount of water is used. Comparably TEM and XRD results indicated the particles diameter of AP-MgO to be 6–35 and 6–13 nm, respectively. XRD spectra of AP-$Al(OH)_3$ and AP-Al_2O_3 indicated an amorphous pattern due to peak broadening with the particle diameter in the range of 2–17 nm (Table 2). Nanoparticle diameter of AP-$Ca(OH)_2$ and AP-CaO was found to be 8–17 and 12–24 nm, respectively. However, Klabunde et al. [4] have indicated the particle diameter (on XRD bases) of AP-MgO and AP-CaO to be 4.2 and 7.3 nm, respectively. The amorphous pattern of AP-SiO_2 result the particle diameter of 12–24 nm. The complete study of synthesized AP-metal hydroxides and oxides using SEM/TEM and XRD has clearly indicated that these are 2–75 nm diameter nanoparticles as particles <100 nm in diameter come under the category of nanoparticles/nanomaterials.

IR spectrum of AP-$Mg(OH)_2$ (Fig. 13) indicated strong absorption around 1500 cm^{-1} corresponding to surface carbonates, C–O vibrations of adsorbed methoxide groups at 1080 cm^{-1}, and a complex structure in the C–H region (2800–2950 cm^{-1}), most likely, also associated with the methoxide groups. Two absorption peaks at 3600 cm^{-1} corresponding to associated OH groups and at 3700 cm^{-1} corresponding to isolated surface OH groups are observed. In addition to this a band near 540 cm^{-1} appeared, which is indicative of Mg–O bond. Mel'gunov et al. [24] have also reported the similar observations. IR spectra of AP and CM-MgO were found to be similar. Negligible intensity peaks at 1080 and 2800–2950 cm^{-1} with AP-MgO clearly indicated the removal of methoxide groups by heat treatment at 500 °C for the conversion of AP-$Mg(OH)_2$ to AP-MgO. Moreover, IR spectra of all AP and CM metal hydroxides/oxides indicated peaks at 1500 cm^{-1} (surface carbonates), 1080 cm^{-1} (C–O) and 2800–2950 cm^{-1} (C–H of methoxide groups), 3600 cm^{-1} (associated OH groups) and 3700 cm^{-1} (isolated surface OH groups). TGA of AP-$Mg(OH)_2$ (Fig. 14) indicated the total weight loss of 46%, but theoretically it should be 31% for conversion of AP-$Mg(OH)_2$ to AP-MgO. Higher loss with AP-$Mg(OH)_2$ was due to the availability of remaining $-OCH_3$ groups and chemisorbed water. The two weight losses, from room temperature to 150 °C (loss of physisorbed water) and from 300 to 400 °C due to loss of chemisorbed water, and decomposition of $-OCH_3$ groups were observed.

Table 3 represents the acid/base neutralization capacity of synthesized and commercial materials. It indicates that when 20 mg of AP-$Mg(OH)_2$ or AP-$Ca(OH)_2$ are added to the distilled water of pH 6.5, the pH increased to 11.4 and 11.9 respectively and to bring the pH back to 6.5 it required 1380.4 and 1386.5 mmol of hydrochloric acid per mole of material under investigation. However, AP-$Al(OH)_3$ showed the decrease in pH from 6.5 to 5.8 indicated it to be slightly acidic. Among AP-metal oxides highest acid requirement was shown by AP-MgO (1532.3 mmol/mol) followed by AP-CaO (911.6 mmol/mol). AP-Al_2O_3 also showed basicity requiring 2.92 mmol of acid per mole of AP-Al_2O_3, whereas, AP-SiO_2 has shown acidic character with the requirement of 3.3 mmol of sodium hydroxide per mole of silicon dioxide nanoparticles. Therefore, the study has indicated

that when acid/base is added to the aqueous solution of prepared nanoparticles initially it reaches to the nanoparticle aggregates and adsorbed, followed by chemisorption, i.e., permanent bonding or neutralization. Commercial metal oxides showed higher basicity (Table 3) in comparison to metal oxide nanoparticles. The order of basicity was found to be CM-MgO > CM-CaO > CM-Al_2O_3. CM-Al_2O_3 was found to be basic requiring 8.85 mmol of acid per mole of it, whereas, CM-SiO_2 showed acidic character as that of AP-SiO_2. Overall the order of basicity was found to be CM-MgO > AP-MgO > CM-CaO > AP-$Ca(OH)_2$ > AP-$Mg(OH)_2$ > AP-CaO > CM-Al_2O_3 > AP-Al_2O_3 > CM-SiO_2 > AP-SiO_2 > AP-$Al(OH)_3$.
Bulk density of synthesized nanoparticles was found to be much less than the material available commercially. This was because of their fluffy and powdery nature. All prepared nanoparticles indicated bulk densities within 0.026–0.098 g/mL (Table 3). AP-$Mg(OH)_2$ showed the lowest value, i.e., 0.026 g/mL. Bulk density of AP-MgO was found to be 0.054 g/mL, which is one fourth of that of commercially available CM-MgO (0.209 g/mL). Moisture content of synthesized nanoparticles was found to be <2.1% (Table 3), however, commercial material indicated to be 2.3–4.2%. AP-Al_2O_3 and AP-$Ca(OH)_2$ showed the lowest and highest values of moisture content, i.e., 0.6 and 2.1%, respectively. Lower moisture content with synthesized nanoparticles was because of super critical drying and heat treatment, which are important steps of their synthesis.

3.2. Kinetics of adsorption of DEClP

To illustrate the kinetics of adsorption of DEClP, percentage weight gain of adsorbate was plotted versus time (t) and represented graphically in Fig. 15. Fig. 15 shows the similar shape of DEClP adsorption uptake curves and different adsorption rates for studied nanoparticles. Fig. 15 was used to compute the equilibration time {the time at which the adsorption ceases (adsorption and desorption are in equilibrium), i.e., no change in weight gain with respect to time} and equilibration capacity (amount of adsorbate in mg/g of adsorbent at equilibration time), and the values have been tabulated in Table 4. At initial stage the rate of adsorption was fast, which gradually slowed down to a steady state at later intervals of time. AP-MgO started with the fastest rate, whereas AP-SiO_2 with the slowest rate of adsorption at initial intervals of time. But AP-SiO_2 crossed AP-CaO and AP-Al_2O_3 at 135 and 230 h respectively and ended with the equilibrium capacity of 885 mg/g. Highest value of equilibration time (380 h, Table 4) was found with AP-SiO_2. AP-MgO nanoparticles showed the highest equilibration capacity (1011 mg/g) among studied systems, this was even higher than AP-SiO_2 (885 mg/g), which had the maximum surface area. This was not in agreement with the statement, higher the surface area higher will be the adsorption capacity. Moreover, AP-SiO_2 showed 1:1 ratio of adsorption potential Vs surface area, whereas, other systems showed >2:1 ratio. Apart from AP-MgO all nanoparticles showed the equilibrium capacity in a similar trend as that of surface area values. Interestingly, AP-CaO with one third of surface area (407.8/3 = 134.8 m^2/g) of AP-MgO showed 70% of adsorption potential than that of AP-MgO.

The study indicated that the transport of DEClP into nanoadsorbent systems is a complex process. It is quite evident from the fact that alumina nanoparticles contain wide pore size distribution, which makes the analysis of adsorption kinetics more complex. The adsorption process involves diffusion in slit shaped micropores with pore widths considerably smaller than the mean free path of the gas molecules at atmospheric pressure [18]. It is likely that processes such as molecular diffusion, Knudsen diffusion, surface diffusion, diffusion in micropores and the chemical interaction of DEClP with the functional groups of nanoparticles and the impregnants in it could all make contributions to the adsorption kinetics.

Modeling of kinetic process being difficult due to wide pore size distribution, the two simple approaches are to use either Ficks diffusion laws for homogeneous materials or to describe the process by Phenomenological model. Although, the particles under study are not homogeneous and spherical, if we assume surface concentration of gas to be constant and that diffusion is controlled by the concentration gradient through the granule then the kinetics of the diffusion can be expressed by the following empirical diffusion equation [16,17].

$$\frac{M_t}{M_e} = K\,t^n \tag{1}$$

where M_t = gas uptake at time t, M_e = gas uptake at equilibrium, K = constant, t = time and n = diffusional exponent.

A graph of log M_t/M_e against log t (Fig. 16) was found to be a straight line at shorter intervals of time and the plots deviated from linearity for all the systems at higher t values. This deviation can be ascribed to the wide pore size distribution of prepared nanoparticles (Fig. 4). The diffusional exponent (n) values were computed by using the slope of straight line in Fig. 16. Diffusional exponent, n being in between 0.5 and 1.0 indicated the diffusion mechanism to be anomalous [15]. The value for constant K, adsorbate–adsorbent interaction coefficient was determined from the intercept of straight line on Y-axis. The K values were more or less the result of adsorption kinetics at lower t values. In present study the highest and lowest values of K (0.17 and 0.05 h^{-1}) was shown by AP-MgO and AP-SiO_2 nanoparticles, respectively. Highest values of constant K with AP-MgO indicated the fastest adsorption kinetics. AP-SiO_2 system with least value of K indicated the slowest adsorption kinetics at lower t values (Fig. 15), while at later intervals of time it crossed AP-Al_2O_3 and AP-CaO, and showed higher adsorption potential (equilibration capacity) than that of AP-Al_2O_3 and AP-CaO. AP-Al_2O_3, AP-MgO and AP-CaO nanoparticles with nearer values of equilibration time showed a small difference in K value, which may be within the experimental precision.

The gas uptake into nanoparticles may be considered as a pseudo-first order mass transfer between the gas phase and the adsorption sites [16,18]. The following phenomenological model, which is equivalent to a linear driving force mass transfer model, can represent the rate of uptake of toxicant.

$$\frac{M_t}{M_e} = 1 - e^{kt} \tag{2}$$

where k is rate constant.

Plots of $\ln(1 - M_t/M_e)$ against time t (Fig. 16) result a straight line, which clearly indicated that the adsorption of DEClP on nanoparticles follows LDF mass transfer kinetic model. Pore size distribution being wide in the studied systems could not adversely affect the applicability of the LDF model at initial intervals of time; however, at longer intervals of time, the curves obtained by making use of the LDF model deviated from linearity, questioning its applicability. Nevertheless, the initial linear portions can be used to evaluate the adsorption parameters, which make the LDF model persuasive. Using LDF model the adsorption kinetics can be compared in terms of the rate constant (k), which indicates the rate of adsorption of DEClP as the system approaches to equilibrium. Rate constant, k can either be determined from the gradient of the kinetic plot as shown in Fig. 17 or by fitting the adsorption uptake curves to Eq. (2). Lowest value of k (6.8×10^{-3} h^{-1}) with AP-SiO_2 was because of Fig. 16, which more or less represents the adsorption kinetics at lower t values. Highest equilibration time with this system also lowered the rate constant at initial time intervals. Based on these results it can be inferred that AP-MgO nanoparticles (with maximum adsorption potential minimum equilibration time and considerable values of k/K) is the best system for the removal

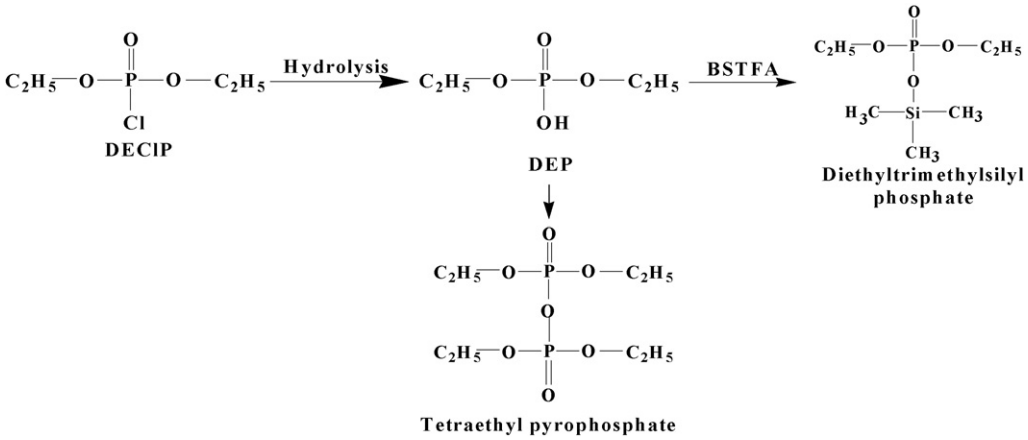

Scheme 1. Degradation products of DEClP on prepared nanoparticles.

of DEClP from simulated contaminated zones (as DEClP vapors in closed glass chamber).

3.3. Identification of reaction products

DEClP indicated the formation of corresponding acids as hydrolysis products (Scheme 1) on prepared systems [6]. DEClP was found to be converted to diethylphosphate, which was detected as diethyltrimethylsilyl phosphate (Fig. 18 and Scheme 1) after silylation with BSTFA {N, O-bis-(trimethylsilyl)-trifluoro acetamide}. The formation of tetraethyl pyrophosphate was also observed (Fig. 19) as degradation product of DEClP. All prepared nanoparticles showed the similar reaction products.

4. Conclusions

Nanoparticles of AP-$Mg(OH)_2$, AP-$Ca(OH)_2$, AP-$Al(OH)_3$ and AP-SiO_2 with surface area in the range of 134.8–904.8 m^2/g were synthesized using aerogel route (bottom-up wet chemical method) with toluene/methanol ratio of 1.96 and supercritical drying. Heat treatment of hydrated precursors at 500 °C yielded the desired metal oxide nanoparticles (AP-MgO, AP-CaO, AP-Al_2O_3 and AP-SiO_2) with surface area of 134.8–887.3 m^2/g. These nanoparticles were found to be mesoporous in nature with high pore volumes than their commercial counter parts. Thus produced metal hydroxide/oxide nanoparticles were characterized for its physical and chemical properties using several analytical techniques. SEM/TEM analysis used to analyze the morphology of the metal oxide nanoparticles indicated them to be having porous web like structures with wide particle size distributions and nanoparticles diameters in the range of 3–75 nm. Utilizing X-ray diffraction pattern and Scherrer formula the particle size of nanoparticles was determined and found to be 2–24 nm. EDX study indicated the presence of carbon with AP-CaO nanoparticles. IR spectra of AP and CM metal hydroxides/oxides indicated peaks at 1500 cm^{-1} (surface carbonates), 1080 cm^{-1} (C–O) and 2800–2950 cm^{-1} (C–H of methoxide groups), 3600 cm^{-1} (associated OH groups) and 3700 cm^{-1} (isolated surface OH groups). TGA profile of synthesized AP-$Mg(OH)_2$ indicated the removal of physisorbed water (<150 °C), chemisorbed water and decomposition of $-OCH_3$ groups (300–400 °C).

Highest value of equilibration time (380 h) was found with AP-SiO_2. AP-MgO nanoparticles showed the highest equilibration capacity (1011 mg/g) among studied systems, this was even higher than AP-SiO_2 (885 mg/g), which had the maximum surface area. Diffusional exponent, n being in between 0.5 and 1.0 indicated the diffusion mechanism to be anomalous. Highest and lowest values of K (0.17 and 0.05 h^{-1}) were shown by AP-MgO and AP-SiO_2 nanoparticles, respectively. Lowest value of k (6.8×10^{-3} h^{-1}) was found to be with AP-SiO_2. DEClP was found to be hydrolyzed on prepared nanoparticles. Conclusively, based on these results it can be inferred that AP-MgO nanoparticles (with maximum adsorption potential minimum equilibration time and considerable values of k/K) can promisingly be used in toxicant decontamination devices.

Acknowledgements

We thank Shri J.C. Kapoor, Director, CFEES, Delhi for providing lab facilities to carry out and publish this work. We also thank Ms. Meenakshi Gupta and Dr. R.P. Singh for useful suggestions.

References

[1] The Environmental Assessment and Management (TEAM) Guide, US Army Corps of Engineers, Engineer Research and Development Center, CERL special report 96/07, October 1995, revised February 2000, http://www.p2pays.org/ref/24/23890.pdf.
[2] I. Campos, L. Gil, R. Martínez-Mañez, J. Soto, J.L. Vivancos, Use of a voltammetric electronic tongue for predicting levels of nerve agent mimics, Proceedings of the Eurosensors XXIII Conference, Procedia Chemistry 1 (2009) 325–328.
[3] R. Richards, R.S. Mulukutla, I. Mishakov, V. Chesnokov, A. Volodin, V. Zaikovski, N. Sun, K.J. Klabunde, Nanocrystalline ultra high surface area magnesium oxide as a selective base catalyst, Scr. Mater. 44 (8–9) (2001) 1663–1666.
[4] K.J. Klabunde, J. Stark, O. Koper, C. Mohs, D.G. Park, S. Decker, Y. Jiang, I. Lagadic, D. Zhang, Nanocrystals as stoichiometric reagents with unique surface chemistry, J. Phys. Chem. 100 (1996) 12142–12153.
[5] M. Winter, D. Hamal, X. Yang, H. Kwen, D. Jones, S. Rajagopalan, K.J. Klabunde, Defining reactivity of solid sorbents: what is the most appropriate metric, Chem. Mater. 21 (12) (2009) 2367–2374.
[6] A. Saxena, A.K. Srivastava, B. Singh, A.K. Gupta, M.V.S. Suryanarayana, P. Pandey, Kinetics of adsorptive removal of DEClP and GB on impregnated Al_2O_3 nanoparticles, J. Hazard. Mater. 175 (2010) 795–801.
[7] G.W. Wagner, L.R. Procell, S. Munavalli, ^{27}Al, ^{47}, ^{49}Ti, ^{31}P, and ^{13}C MAS NMR study of VX, GD, and HD reactions with nanosize Al_2O_3, conventional Al_2O_3 and TiO_2, and aluminum and titanium metal, J. Phys. Chem. C 111 (47) (2007) 17564–17569.
[8] K.J. Klabunde, Nanoscale Materials in Chemistry, John Wiley and Sons, New York, 2001.
[9] S. Utamapanya, K.J. Klabunde, J.R. Schlup, Nanoscale metal oxide particles/clusters as chemical reagents. Synthesis and properties of ultrahigh surface area magnesium hydroxide and magnesium oxide, Chem. Mater. 3 (1991) 175–181.
[10] A. Saxena, B. Singh, A. Sharma, V. Dubey, R.P. Semwal, M.V.S. Suryanarayana, V.K. Rao, K. Sekhar, Adsorption of dimethylmethylphosphonate on metal impregnated carbons under static conditions, J. Hazard. Mater. 134 (1–3) (2006) 104–111.
[11] A. Saxena, A.K. Srivastava, B. Singh, Kinetics of adsorption of 2-CEES and HD on impregnated silica nanoparticles under static conditions, AIChE 55 (5) (2009) 1236–1245.
[12] A. Saxena, A.K. Srivastava, A. Sharma, B. Singh, Kinetics of adsorption of 2-chloroethylethylsulphide on Al_2O_3 nanoparticles with and without impregnants, J. Hazard. Mater. 169 (2009) 419–427.

[13] G.K. Prasad, B. Singh, A. Saxena, Kinetics of adsorption of sulfur mustard vapors on carbons under static conditions, AIChE 52 (2) (2006) 678–682.
[14] J. Crank, The Mathematics of Diffusion, Clerendon Press, Oxford, 1956.
[15] C.R. Reid, I.P.O. Koye, K.M. Thomas, Adsorption of gases on carbon molecular sieves used for air separation: spherical adsorptives as probes for kinetic selectivity, Langmuir 14 (9) (1998) 2415–2425.
[16] N.J. Foley, K.M. Thomas, P.L. Forshaw, D. Stanton, P.R. Norman, Kinetics of water vapour adsorption on active carbon, Langmuir 13 (7) (1997) 2083–2084.
[17] K.F. Loughlin, M.M. Hassan, A.I. Fatehi, M. Zahur, Rate and equilibrium sorption parameters for nitrogen and methane on carbon molecular sieve, Gas Sep. Purif. 7 (4) (1993) 264–273.
[18] H.K. Chagger, F.E. Ndaji, M.L. Sykes, K.M. Thomas, Kinetics of adsorption and diffusional characteristics of carbon molecular sieves, Carbon 33 (10) (1995) 1405–1411.
[19] J.-M. Lin, H.-H. Li, A.-M. Zhou, Synthesis of benzyl/allyl alkyl ethers from corresponding magnesium alkoxides, Tetrahedron Lett. 37 (29) (1996) 5159–5160.
[20] C.L. Carnes, K.J. Klabunde, Unique chemical reactivities of nanocrystalline metal oxides toward hydrogen sulfide, Chem. Mater. 14 (4) (2002) 1806–1811.
[21] K.T. Ranjit, K.J. Klabunde, Solvent effects in the hydrolysis of magnesium methoxide, and the production of nanocrystalline magnesium hydroxide. An aid in understanding the formation of porous inorganic materials, Chem. Mater. 17 (1) (2005) 65–73.
[22] O. Busmundrud, Vapour breakthrough in activated carbon beds, Carbon 31 (2) (1993) 279–286.
[23] Y. Diao, W.P. Walawender, C.M. Sorensen, K.J. Klabunde, T. Ricker, Hydrolysis of magnesium methoxide. Effects of toluene on gel structure and gel chemistry, Chem. Mater. 14 (1) (2002) 362–368.
[24] M.S. Mel'gunov, V.B. Fenelonov, E.A. Mel'gunova, A.F. Bedilo, K.J. Klabunde, Textural changes during topochemical decomposition of nanocrystalline $Mg(OH)_2$ to MgO, J. Phys. Chem. B 107 (11) (2003) 2427–2434.